Nano Research 2016, 9(10): 3099–3115
DOI 10.1007/s12274-016-1193-8
Research Article
ISSN 1998-0124
CN 11-5974/O4

Morphology-selective synthesis of active and durable gold catalysts with high catalytic performance in the reduction of 4-nitrophenol

Daowei Gao[1], Xin Zhang[1] (✉), Xiaoping Dai[1], Yuchen Qin[1], Aijun Duan[1] (✉), Yanbing Yu[1], Hongying Zhuo[1], Hairui Zhao[1], Pengfang Zhang[1], Yan Jiang[1], Jianmei Li[2], and Zhen Zhao[2]

[1] *State Key Laboratory of Heavy Oil Processing, China University of Petroleum, Beijing 102249, China*
[2] *College of Science, China University of Petroleum, Beijing 102249, China*

Received: 13 May 2016
Revised: 26 June 2016
Accepted: 29 June 2016

KEYWORDS
gold catalysis,
porous material,
environmental pollution,
4-nitrophenol

ABSTRACT

A series of novel catalysts consisting of nanosized Au particles confined in micro-mesoporous ZSM-5/SBA-15 (ZSBA) materials with platelet (PL), rod (RD), and hexagonal-prism (HP) morphologies have been synthesized *in situ*. These catalysts possess both SBA-15 and ZSM-5 structures and exhibit excellent stability of their active sites by confinement of the Au nanoparticles (NPs) within ZSBA. The catalysts have been characterized in depth to understand their structure–property relationships. The gold NP dimensions and the pore structure of the catalysts, which were found to be sensitive to calcination temperature and synthetic conditions, are shown to play vital roles in the reduction of 4-nitrophenol. Au/ZSBA-PL, with short mesochannels (210 nm) and a large pore diameter (6.7 nm), exhibits high catalytic performance in the reduction of 4-nitrophenol, whereas Au/ZSBA-HP and Au/ZSBA-RD, with long mesochannels and relatively smaller pore sizes, show poor catalytic activities. In the case of catalysts with different gold NP sizes, Au/ZSBA-PL-350 with an Au NP diameter of 4.0 nm exhibits the highest reaction rate constant (0.14 min^{-1}) and turnover frequency (0.0341 s^{-1}). In addition, the effect of the reaction parameters on the reduction of 4-nitrophenol has been systematically investigated. A possible mechanism for 4-nitrophenol reduction over the Au/ZSBA catalysts is proposed.

1 Introduction

Pollution of the environment by industrial toxic organic materials entails very serious health hazards for all living species in nature [1–6]. In recent years, researchers in chemistry have been putting in increasing efforts to overcome this problem. Green and sustainable development can be achieved through

Address correspondence to Xin Zhang, zhangxin@cup.edu.cn; Aijun Duan, duanaijun@cup.edu.cn

chemical transformations using nontoxic chemicals and green solvents [7–10]. For this purpose, the disposal of nitroaromatic compounds is currently an area of intensive research [11–13]. Among them, nitrophenol compounds are the most common organic pollutants in industrial waste and are often stable at room temperature. Particularly, 4-nitrophenol (4-NP) is a notorious industrial pollutant that shows excellent solubility and stability in water [14–16]. The disposal of 4-NP can be realized through various methods, including electrocoagulation, microbial degradation, catalytic reduction, and catalytic oxidation [17–20]. Among them, the catalytic reduction of 4-NP is regarded as the most efficient and economical disposal method, and the corresponding product, 4-aminophenol (4-AP), can be reused in the synthesis of aniline and in paracetamol production [21, 22]. Therefore, the exploration of novel catalysts with highly effective and stable performance for the reduction of nitro-compounds in aqueous solution at ambient reaction conditions remains an important task.

Noble metal catalysts (such as Au, Ag, Pd, PdCu, PtNi, AuCu) with outstanding catalytic performance have attracted significant attention for the reduction of nitro-compounds [23–25]. Nevertheless, the interaction between the noble metal nanoparticles (NPs) and the support is often not strong enough, and agglomeration or leaching of the NPs often occurs during the reaction. The encapsulation of the metals in micropore zeolites can protect such metal clusters from leaching [26]. However, the confinement of these noble metal clusters within micropore zeolites cannot effectively catalyze large molecules due to the restrictions imposed by the small pore sizes. Solid supports, such as KIT-6, SBA-15, MCM-41, and FDU-12, are considered excellent supports for noble metal catalysts [27]. Their high surface area and pore size contribute to the dispersion of noble metal particles and the diffusivity of the reactants towards the catalysts. Therefore, the incorporation of noble-metal@micropore-zeolite particles into the walls of mesoporous materials results in stable noble-metal NPs and excellent diffusivity of the reactants. In addition to the pore size and surface area, the pore structure and morphology of the supports can also influence the catalytic activity. For instance, in our previous work [4], we prepared NiMo catalysts supported on a mesoporous material (Al-SBA-15) with different morphologies, and the catalytic results showed that the activity of DBT HDS over these catalysts followed the order: long-rod-shaped catalyst < hexagonal-prism-shaped catalyst < sphere-shaped catalyst. Katiyar et al. [28] also found that the saturation capacity towards the adsorption of proteins over SBA-15 particles with spherical morphology was higher than that of fibrous particles. The morphology of the support has an important effect on the dispersion of the active metal species, which can further affect the catalytic performance of the corresponding catalyst [29, 30]. Moreover, the morphology and pore size of the support are also crucial factors for the diffusion of reactants and products in the channels during the reaction. Therefore, the encapsulation of noble metals within micro-mesoporous zeolites with different morphologies and pore structures is of great significance.

In this work, we have used a mercaptosilane-assisted method to fabricate Au nanoparticles within micro-mesoporous ZSBA (ZSM-5/SBA-15) materials with different morphologies. First, the Au/ZSM-5 seeds were prepared using a bifunctional ligand ((3-mercaptopropyl)trimethoxysilane) as an assistant. Secondly, Au/ZSBA samples with different morphologies were synthesized via encapsulation of the Au/ZSM-5 seeds in the mesoporous silica framework of SBA-15 under different synthetic conditions. The physicochemical properties of the as-synthesized catalysts were characterized through various techniques. The catalytic activity of Au/ZSBA was evaluated for the reduction of 4-NP. The effects of the gold nanoparticle size, the support morphology, and the reaction parameters on the reduction of 4-NP were systematical investigated. In addition, a possible reaction mechanism for the reduction of 4-NP over the Au/ZSBA catalysts is proposed.

2 Experimental

2.1 Catalyst preparation

Au/ZSBA catalysts with different morphologies were synthesized by the following procedure, as shown in Scheme 1. First, a solution of zeolite seed Au/ZSM-5

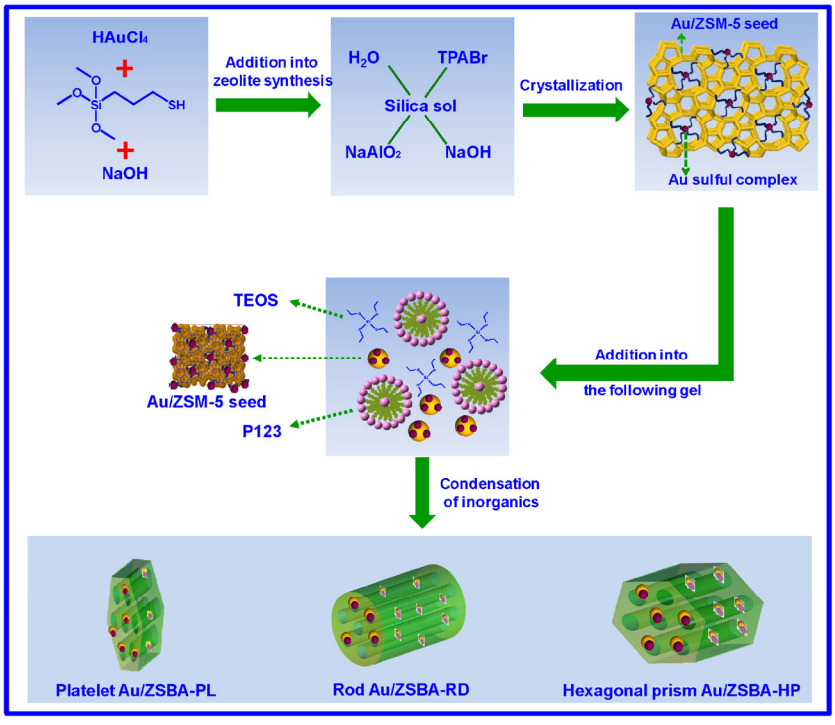

Scheme 1 Schematic representation of the preparation process for Au/ZSBA with different morphologies.

was synthesized by hydrothermal crystallization in the presence of (3-mercaptopropyl)-trimethoxysilane. The typical synthetic steps for the Au/ZSM-5 seeds were carried out as follows: (3-mercaptopropyl)-trimethoxysilane (0.24 g) and NaOH (0.3 g) were dissolved in 5.0 g of deionized H_2O. A solution of 0.075 g of $HAuCl_4{\cdot}4H_2O$ in 2.1 g of H_2O was added to the previous solution under stirring to form solution I. Solution II was prepared by mixing 0.25 g of $NaAlO_2$, 0.6 g of NaOH, 15.0 g of colloidal silica, and 2.71 g of tetrapropyl-ammonium bromide (TPABr, added dropwise) in 20.0 g of deionized H_2O. Then, solution I was mixed with solution II and the resulting reaction mixture was further stirred for 4 h. The resultant gel was then transferred into a polypropylene bottle and hydrothermally crystallized at 443 K without stirring for 4.5 h to obtain the Au/ZSM-5 zeolite seeds. Secondly, Au/ZSBA materials with different morphologies were prepared using tetraethylorthosilicate (TEOS) and Au/ZSM-5 seeds as the silicon source. P123 (2 g) was dissolved in a hydrochloric acid solution, and the Au/ZSM-5 seeds and TEOS were added dropwise into the above mixture with stirring. The above mixture was stirred at 40 ˚C for 1 h and further maintained under static conditions for 24 h. Then, the gel solution was transferred into a teflon bottle and hydrothermally crystallized at 100 ˚C for 24 h. The synthetic process for rod Au/ZSBA was similar to that of hexagonal-prism Au/ZSBA, however glycerol was added as a co-solvent. A certain amount of $ZrOCl_2{\cdot}8H_2O$ was also added to the mixed solution during the synthesis of platelet Au/ZSBA, and the stirring temperature was controlled at 35 ˚C. Finally, Au/ZSBA materials with different morphologies were obtained by filtering and drying at room temperature. The P123 template was removed by extraction with ethanol. The removal of (3-mercaptopropyl)trimethoxysilane was carried out by heating the samples from ambient temperature to 623 K, and then holding for 3 h. The synthesized materials were denoted as Au/ZSBA-HP (hexagonal-prism), Au/ZSBA-RD (rod), and Au/ZSBA-PL (platelet). For comparison, Au/SBA-15 was prepared using the method of incipient wetness impregnation.

2.2 Catalyst characterization

The morphology of the materials was observed by field emission scanning electron microscopy (FESEM) on a Quanta 200F instrument using accelerating voltage

at 20 kV. The samples were coated with gold before the FESEM measurements. Transmission electron microscopy (TEM) images were obtained from thin edges of the particles supported on a porous carbon grid with a JEOL JEM 2100 electron microscope operated at 120 kV. High angle annular dark-field imaging-scanning transmission electron microscopy (HAADF-STEM) and energy-dispersive spectrometry (EDS) elemental mapping images were taken with a Tecnai F20 instrument at 200 kV. The low-angle X-ray diffraction (XRD) patterns of the materials were obtained on a Bruker D8 Advance Powder diffractometer using Cu Kα radiation and scattering slits of 0.05°. Wide-angle XRD patterns were measured on a powder X-ray diffractometer (Shimadzu XRD6000) using Cu Kα (λ = 0.15406 nm) radiation and with a scanning rate of 2° per min. Fourier transform infrared spectroscopy (FT-IR) measurements were performed on a FTS-3000 spectrophotometer (American Digilab Company). Raman spectra were obtained with a Renishaw Raman InVia Microscope (Spectra-Physics model 163) operating with an argon ion laser at 244 nm wavelength. The pore size distribution and surface area of the materials were obtained from nitrogen isotherms using a Micromeritics ASAP 2010 system at liquid nitrogen temperature. H_2 temperature- programmed desorption (H_2-TPD) and H_2 temperature- programmed reduction (H_2-TPR) were conducted on a homemade apparatus equipped with a thermal conductivity detector (TCD). Inductively coupled plasma atomic emission spectrometry (ICP-AES) analysis was performed on a PerkinElmer emission spectrometer.

2.3 Catalytic measurements

The reduction of 4-NP over the as-synthesized catalysts was studied in a quartz cuvette and detected using an ultraviolet–visible (UV–vis) spectroscopy (754PC) instrument at room temperature. A total of 2.5 mL of a fresh $NaBH_4$ solution (0.01 M) was mixed with a certain amount of the Au/ZSBA catalysts. Subsequently, 25 μL of an aqueous 4-NP solution (0.01 M) was added to the above solution, and the reduction reaction started. UV spectrometry measurements were conducted to detect the reaction by measuring the absorbance of the solution at different reaction time. The reduction of 4-NP was also conducted under different reaction conditions, by varying the catalyst loading and the concentration of 4-NP and the reducing agent ($NaBH_4$), to determine the effect of these parameters on the reduction of 4-NP. The reduction reaction is summarized in the following equations

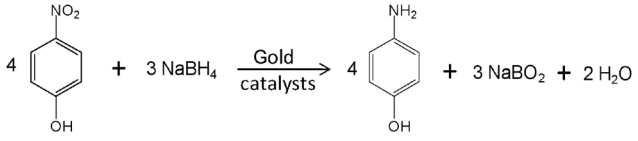

(1)

The conversion of 4-NP is expressed by

$$\text{Conversion}(4-\text{NP}) = \left(1-\frac{A_t}{A_0}\right)\times 100\% \quad (2)$$

where A_t and A_0 are the absorbance of 4-nitrophenolate at time t and 0, respectively.

According to Ref. [1], the experimental results of the reduction of 4-NP over supported gold catalysts point towards pseudo-first order kinetics. Therefore, in this research, the catalytic activity was assumed to follow pseudo-first order kinetics according to the equations below

$$k = \frac{-\ln(C_t / C_0)}{t} \quad (3)$$

$$K = \frac{k}{m} \quad (4)$$

where k and K are the rate constants of the reaction in min^{-1} and $min^{-1}\cdot g^{-1}$, respectively, C_t and C_0 denote the 4-NP concentration at time t and 0, respectively, and m is the catalyst mass in g.

3 Results and discussion

3.1 Characterization of Au/ZSBA with different morphologies

The low-angle and wide-angle XRD patterns of Au/ZSBA with platelet, hexagonal-prism, and rod morphologies are listed in Figs. 1(a) and 1(b), respectively. It can be seen in Fig. 1(a) that all the Au/ZSBA materials have three well-resolved diffraction peaks, representing the (100), (110), and (200) reflections, respectively, which demonstrates that these materials possess a similar structure to that of a *P6mm* hexagonal

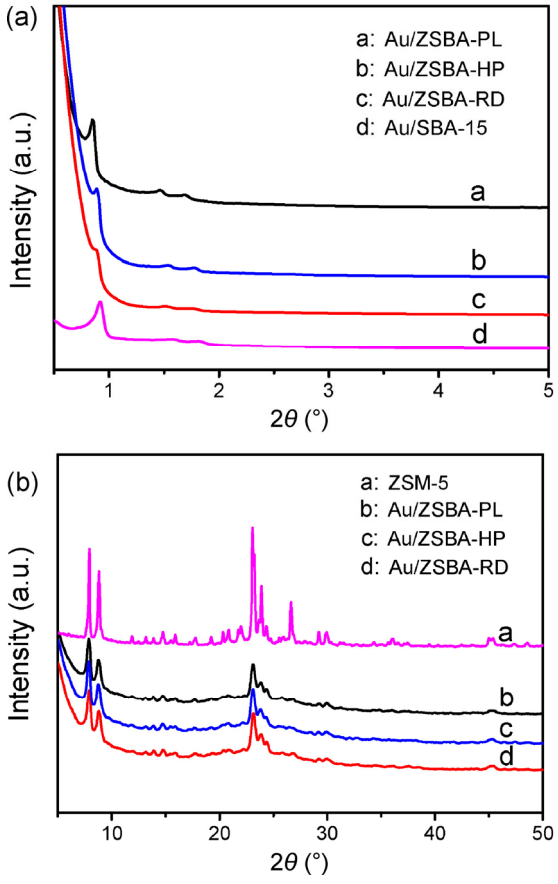

Figure 1 XRD patterns of the Au/ZSBA samples with different morphologies in the (a) low-angle and (b) wide-angle domains.

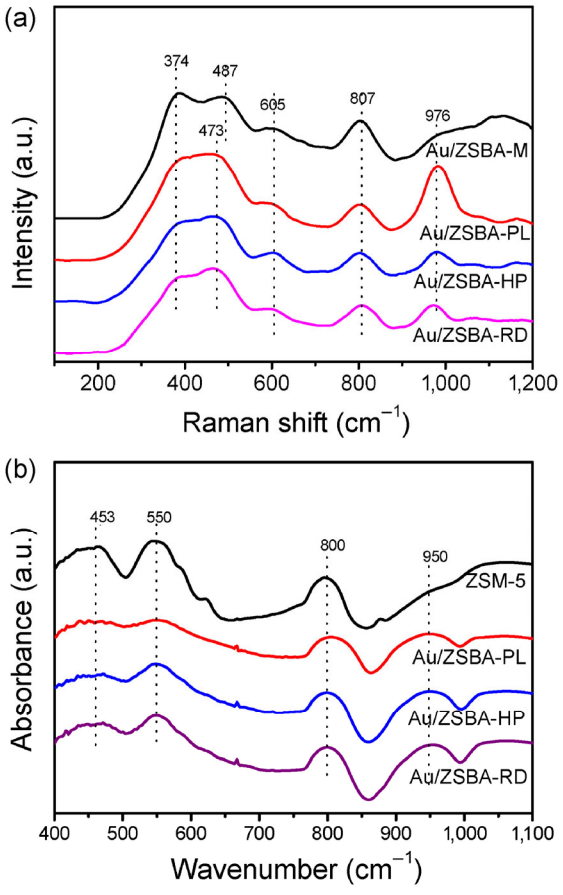

Figure 2 (a) The Raman (excitation at 244 nm, laser power 4.0 mA) and (b) FT-IR spectra of the as-synthesized materials with different morphologies. Au/ZSBA-M denotes the physical mixture of Au/ZSM-5 and SBA-15.

mesoporous material [31]. The wide-angle XRD patterns shown in Fig. 1(b) indicate that the Au/ZSBA materials possess the same characteristic peaks than zeolite ZSM-5 in the 2θ range of 8°–10° and 20°–25°, which is consistent with the typical pattern of an MFI crystal structure. The results of the XRD characterization indicate that the as-synthesized Au/ZSBA catalysts possess both ZSM-5 and SBA-15 structures. Notably, there are no diffraction peaks assignable to gold on the Au/ZSBA XRD patterns, indicating that the size of the gold crystals is below 3 nm and/or beyond the detection limit due to the very low gold loadings used here.

UV Raman spectroscopy measurements with excitation at 244 nm were performed to investigate the coordination environment of the ZSBA framework [32, 33]. As illustrated in Fig. 2(a), five Raman bands at 374, 473, 605, 807, and 976 cm^{-1} are observed for the Au/ZSBA samples with different morphologies. According to Ref. [34], the band at 374 cm^{-1} is assigned to the bending mode of the five-membered rings of the ZSM-5 zeolite. The bands at 473 and 605 cm^{-1} are attributed to the three and four siloxane rings of SBA-15, and the bands at 807 and 976 cm^{-1} are ascribed to the Si–O–Si symmetric stretching and the Si–OH stretching of the surface hydroxyl groups, respectively. It is noteworthy that the position of the band for the three and four siloxane rings for Au/ZSBA (473 cm^{-1}) is different from that of the physical mixture (Au/ZSBA-M) of Au/ZSM-5 and SBA-15 (487 cm^{-1}). Moreover, the peak intensity of the bending mode of the five-membered rings (374 cm^{-1}) in Au/ZSBA-M is higher than that in the Au/ZSBA samples with different morphologies, demonstrating that the coordination environment of the framework in Au/ZSBA is different from that in Au/ZSBA-M. The FT-IR spectra of the as-synthesized materials are shown in Fig. 2(b). It can be observed that the FT-IR spectra consist of

bands at 453, 550, 800, 950, and 1,033 cm^{-1}. The band at 800 cm^{-1} is ascribed to the Si–O–Si symmetric stretching vibration, similar to that of SiO_2-based materials [35]. In addition, the bands at 1,033 and 950 cm^{-1} are assigned to the Si–O–Si asymmetric stretching vibration and the defective Si–OH groups, respectively [35–38]. The band at 453 cm^{-1} represents the vibration of the TO_4 units, and the band centered at 550 cm^{-1} is attributed to the double five rings of the characteristic MFI-type structure (ZSM-5 zeolite) [35], revealing that the Au/ZSBA materials contain ZSM-5 zeolite seeds.

The morphology of Au/ZSBA synthesized under different conditions was investigated by FESEM, and the results are displayed in Fig. 3. The width and length of rod Au/ZSBA are ~280 and ~1,200 nm, respectively, while those of hexagonal-prism Au/ZSBA are ~980 and ~750 nm. The variation in the particle diameter and morphology of Au/ZSBA may be due to the different reagents and conditions in their synthesis.

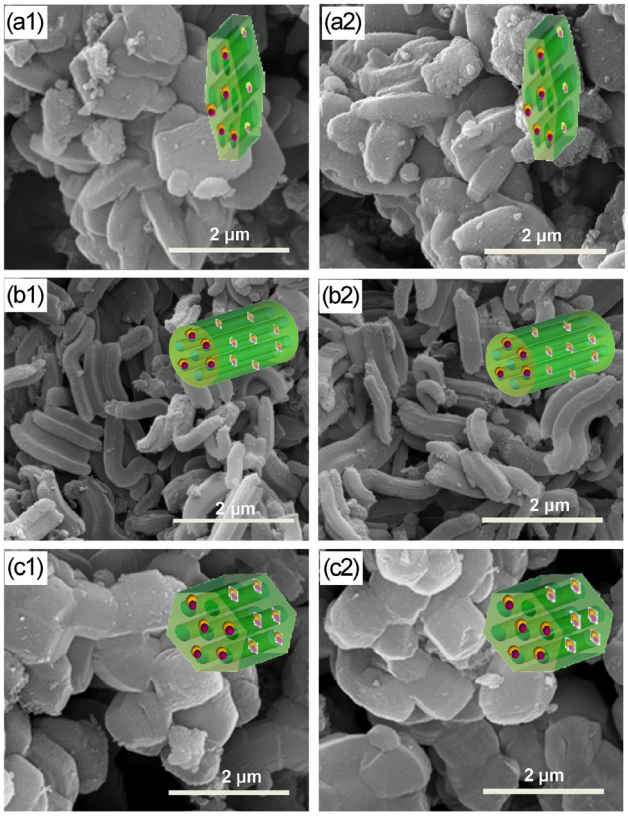

Figure 3 FESEM images of the as-synthesized Au/ZSBA materials with (a) platelet, (b) rod, and (c) hexagonal-prism morphologies. 1 and 2 represent without calcination and after calcination at 350 °C, respectively.

This phenomenon can be ascribed to the local curvature energy at the interface of amphiphilic block copolymer species and inorganic silica. Platelet Au/ZSBA (Figs. 3(a1) and 3(a2)) was prepared by introducing a small amount of Zr(IV) ions in the reaction mixture. The Zr(IV) ions may have two important roles in the synthetic process; they could not only reduce the critical micellar concentration value of the P123 triblock copolymer, but also increase the local concentration of TEOS around the P123 micelles [29]. The rod (Figs. 3(b1) and 3(b2)) and hexagonal-prism (Figs. 3(c1) and 3(c2)) Au/ZSBA samples were synthesized at different temperatures, indicating that the synthesis temperature has an effect on the morphology of Au/ZSBA.

The TEM images and Au size distribution histograms of Au/ZSBA with different morphologies are listed in Fig. 4. All the materials display well-ordered hexagonal arrays of mesopores, which confirms their 2D *P6mm* hexagonal structure, consistent with the XRD results described above. As illustrated in Figs. 4(d) and 4(g), the mesochannels of the hexagonal-prism and rod Au/ZSBA samples run along the length of the particles. The average size of the Au nanoparticles encapsulated in Au/ZSBA-PL, Au/ZSBA-RD, and Au/ZSBA-HP is 4.0, 4.4, and 4.3 nm, respectively, smaller than the pore size of the corresponding materials. In contrast, the gold nanoparticles in the Au/SBA-15 control sample, prepared by incipient wetness impregnation, are located on the external surface of SBA-15 and their size is 9.3 nm, larger than the pore size of the support.

In order to investigate the effect of the calcination temperature on the Au nanoparticle size, the Au/ZSBA-PL catalyst was calcined at 100, 200, 350, and 550 °C, and the obtained catalysts were denoted as Au/ZSBA-PL-100, Au/ZSBA-PL-200, Au/ZSBA-PL-350, and Au/ZSBA-PL-550, respectively. As displayed in Fig. 5, it can be seen that Au/ZSBA-PL-100 and Au/ZSBA-PL-200 exhibit ultrafine gold particles with sizes smaller than 2.2 nm. The average size of the Au nanoparticles in Au/ZSBA-PL-100 and Au/ZSBA-PL-200 are 0.9 and 1.5 nm, respectively, demonstrating that Au/ZSBA-PL possess ultrafine and highly dispersed Au particles at calcination temperatures below 200 °C. The distribution of O, Al, Si, and Au on the surface of the catalysts was characterized by EDS elemental

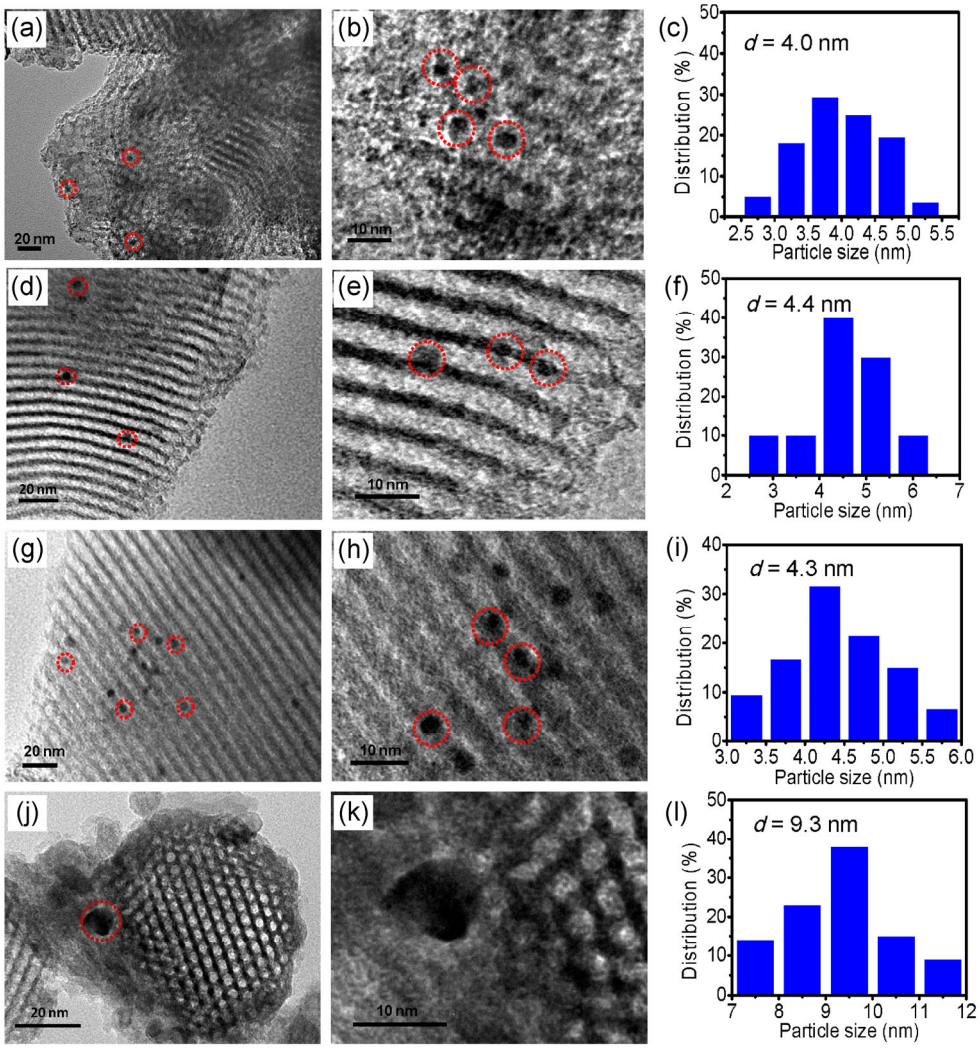

Figure 4 TEM images and Au size distribution histograms of Au/ZSBA with different morphologies. (a)–(c) Platelet Au/ZSBA-PL, (d)–(f) rod Au/ZSBA-RD, (g)–(i) hexagonal-prism Au/ZSBA-HP, and (j)–(l) Au/SBA-15.

mapping analysis. The EDS mapping images of Au/ZSBA-PL-100 (Figs. 5(c)–5(g)) and Au/ZSBA-PL-200 (Figs. 5(j)–5(n)) demonstrate that O, Al, Si, and Au are uniformly distributed in the samples.

Since it is highly difficult to incorporate Al into the framework of SBA-15 under strong acidic conditions, the Al widely distributed in Au/ZSBA-PL must be derived from the Au/ZSM-5 seeds, indicating that the primary and secondary building units of the Au/ZSM-5 zeolite are the construction units of Au/ZSBA-PL. As displayed in Figs. 5 and 6, the average Au particle size of these catalysts follows the order: Au/ZSBA-PL-100 (0.9 nm) < Au/ZSBA-PL-200 (1.5 nm) < Au/ZSBA-PL-350 (4.0 nm) < Au/ZSBA-PL-550 (7.2 nm), demonstrating that the Au particle size in Au/ZSBA-PL increases with the calcination temperature. In particular, the average particle size of gold in Au/ZSBA-PL-550 reaches up to 7.2 nm. It can also be noted from the EDS elemental mapping images of Au included in Figs. 5 and 6 that the gold nanoparticles tend to aggregate when the calcination temperature increases.

UV–vis diffuse reflectance spectroscopy (DRS) is one of the most widely used techniques as a source of complementary information on the size of gold nanoparticles. According to Ref. [39], the absorbance band can be attributed to the plasmon resonance of metallic Au particles. The absorbance intensity of the band is closely related to the particle size and content of Au in Au/ZSBA. Figure 7 shows the UV–vis DRS spectra of Au/ZSBA with different morphologies and

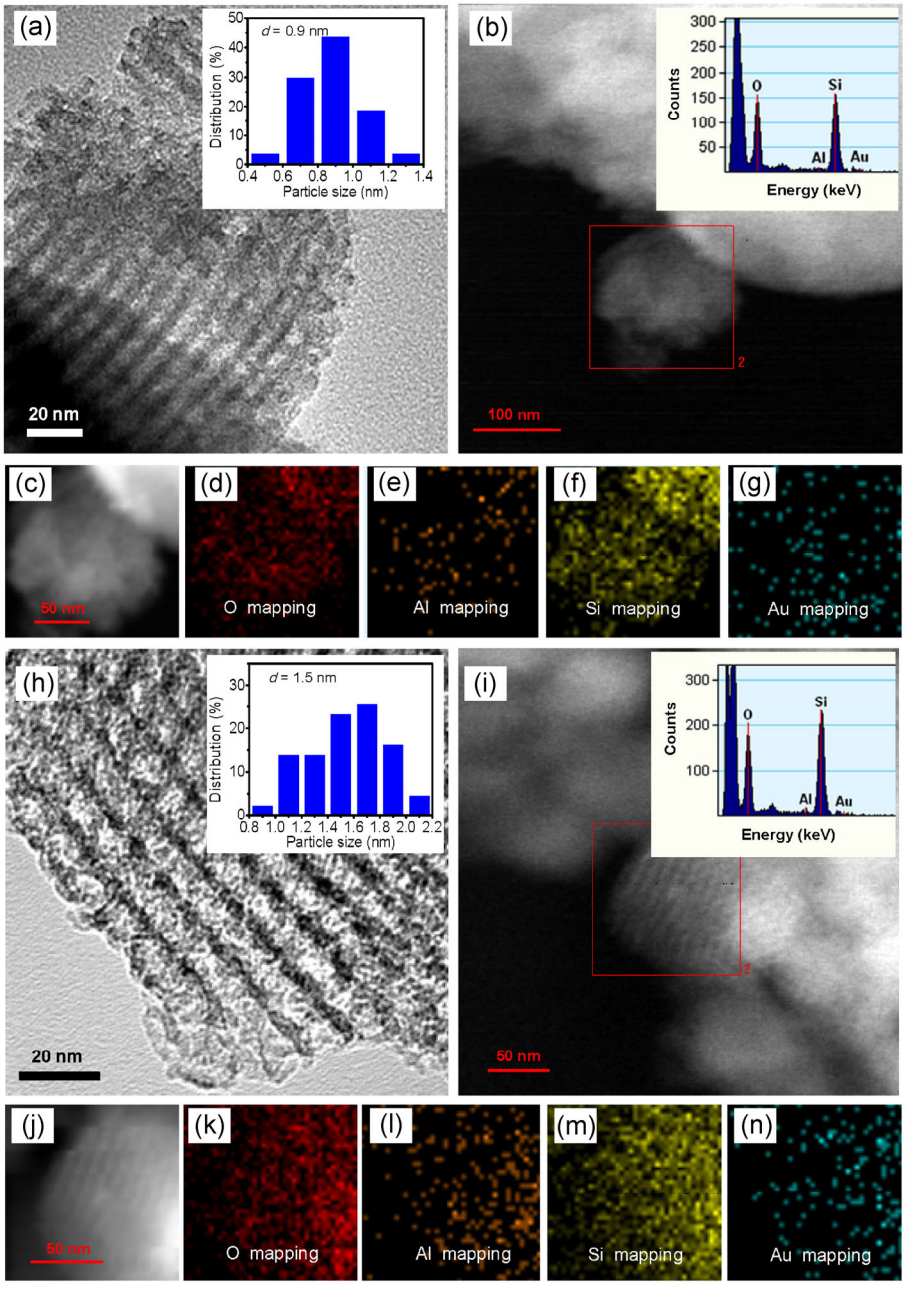

Figure 5 (a) TEM, (b) HAADF-STEM, and (c)–(g) EDS mapping images of Au/ZSBA-PL-100. (h) TEM, (i) HAADF-STEM, and (j)–(n) EDS mapping images of Au/ZSBA-PL-200.

those of Au/ZSBA-PL after calcination at different temperatures. For the Au/ZSBA samples shown in Fig. 7(a), the intensity of the absorbance band of Au/SBA-15 is slightly higher than that of Au/ZSBA-PL, Au/ZSBA-HP, and Au/ZSBA-RD, indicating that the particle size of Au in Au/SBA-15 is larger than that in the different Au/ZSBA samples. The intensity of the absorbance band of the Au particles in Au/ZSBA follows the order: Au/ZSBA-PL < Au/ZSBA-HP < Au/ZSBA-RD. In addition, the absorbance band of the Au particles in Au/SBA-15 and Au/ZSBA appears at 536 and 520 nm, respectively. The red shift for Au/SBA-15 is induced by the different sizes of Au particles [40]. The band at 280 nm in Au/ZSBA-PL, Au/ZSBA-HP, and Au/ZSBA-RD is assigned to the ZSM-5 zeolite seeds. In terms of the Au/ZSBA-PL samples calcined at different temperatures (Fig. 7(b)), the intensity of the absorbance band of the Au

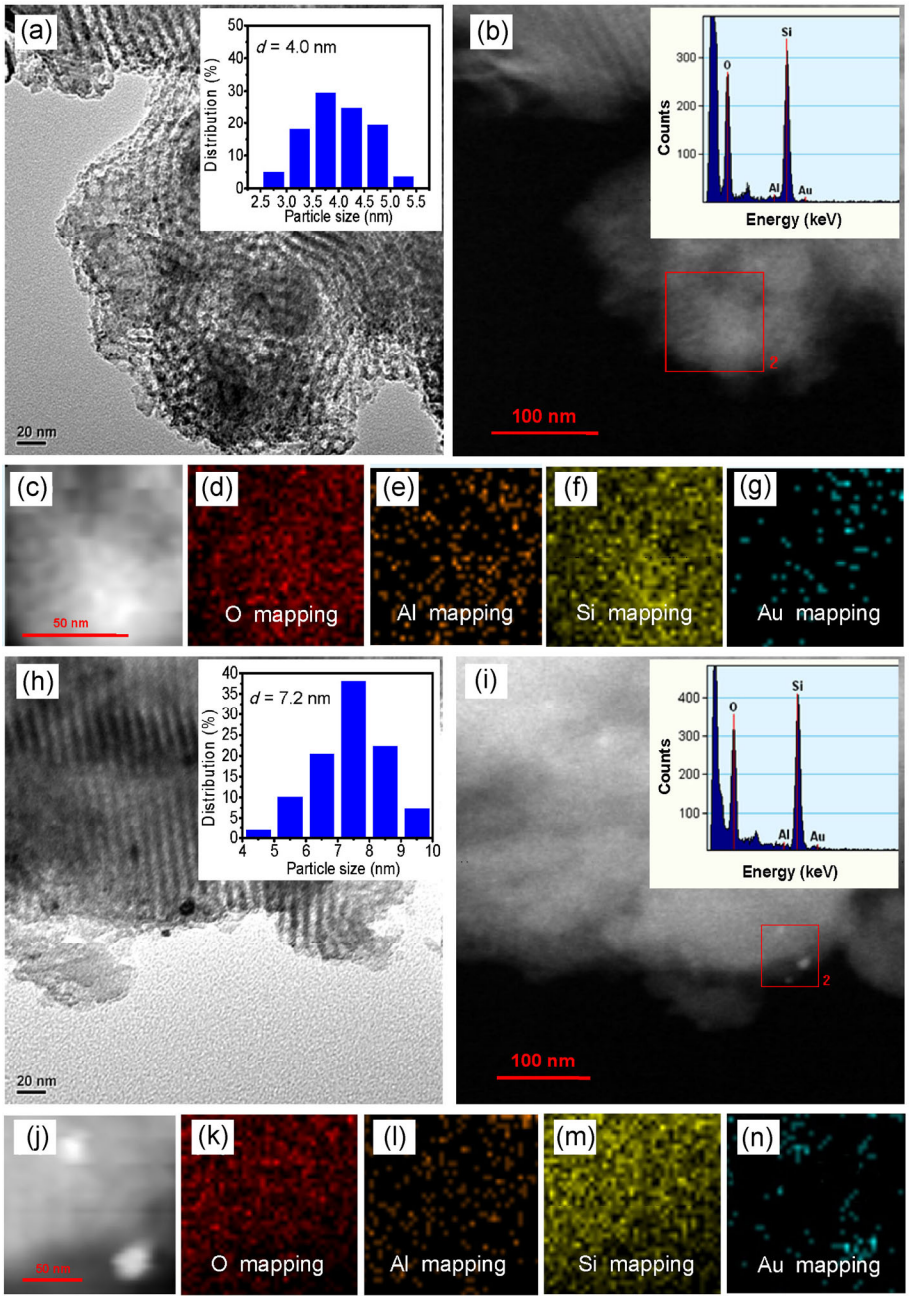

Figure 6 (a) TEM, (b) HAADF-STEM, and (c)–(g) EDS mapping images of Au/ZSBA-PL-350. (h) TEM, (i) HAADF-STEM, and (j)–(n) EDS mapping images of Au/ZSBA-PL-550.

particles in the corresponding catalysts follows the sequence: Au/ZSBA-PL-100 < Au/ZSBA-PL-200 < Au/ZSBA-PL-350 < Au/ZSBA-PL-550. Among them, the almost negligible absorbance intensity of the Au/ZSBA-PL-100 sample is attributed to the very small size of the Au particles, while the relatively strong band intensity for Au/ZSBA-PL-550 is assigned to the increased particle size of Au after calcination at 550 ℃. In addition, there is a red shift of the absorption edge for Au/ZSBA-PL with the increasing calcination temperature. The bands at 225 and 280 nm are attributed to the ZSM-5 zeolite seeds confined in Au/ZSBA-PL [41, 42].

The N_2 adsorption–desorption isotherms and the corresponding pore size distribution curves of Au/SBA-15, Au/ZSBA-PL, Au/ZSBA-HP, and Au/ZSBA-RD

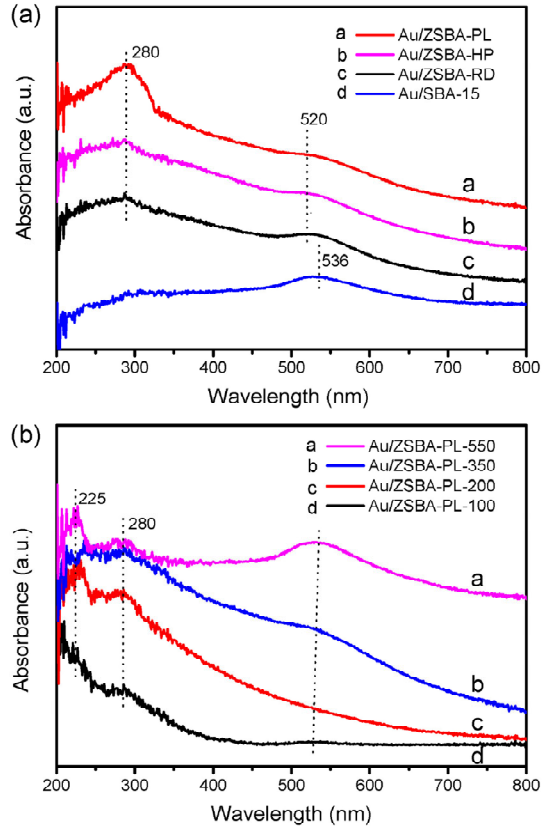

Figure 7 (a) UV–vis DRS spectra of Au/ZSBA with different morphologies and (b) Au/ZSBA-PL after calcination at different temperatures.

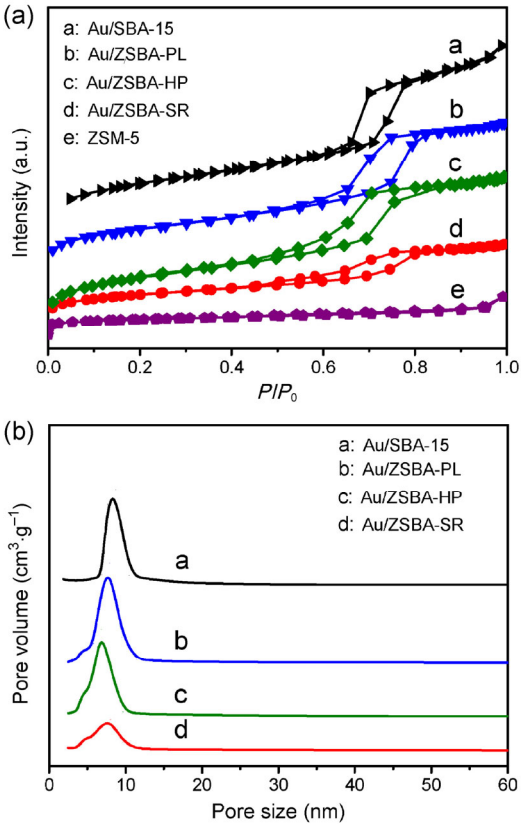

Figure 8 (a) N_2 adsorption–desorption isotherms and (b) pore size distribution curves of the as-synthesized materials: Au/SBA-15, Au/ZSBA-PL, Au/ZSBA-HP, and Au/ZSBA-RD.

are displayed in Figs. 8(a) and 8(b), respectively. All the as-prepared materials exhibit similar type IV isotherms with H1 type hysteresis loops and relatively narrow mesoporous distributions, which are typical characteristics of mesoporous materials [38]. The isotherms of Au/SBA-15, Au/ZSBA-PL, Au/ZSBA-HP, and Au/ZSBA-RD show a sharp inflection in the P/P_0 range from 0.60 to 0.80, which is a typical behavior of capillary condensation within uniform mesostructures. The textural properties of the materials are listed in Table S1 (see the Electronic Supplementary Material (ESM)). The as-synthesized Au/ZSBA catalysts with different morphologies possess different surface areas following the order: Au/ZSBA-RD (433 $m^2 \cdot g^{-1}$) < Au/ZSBA-PL (685 $m^2 \cdot g^{-1}$) < Au/ZSBA-HP (785 $m^2 \cdot g^{-1}$). The corresponding pore diameters of the materials follow the order: Au/ZSBA-HP (5.9 nm) < Au/ZSBA-RD (6.0 nm) < Au/ZSBA-PL (6.7 nm). These data indicate that the introduction of Zr(IV) increases the surface area and the pore diameter of the as-synthesized materials.

H_2-TPD experiments were performed to obtain information about H_2 activation/dissociation over the Au/ZSBA materials. Broad peaks are observed in the range from 120 to 700 °C for Au/ZSBA-PL, Au/ZSBA-RD, and Au/ZSBA-HP (Fig. S1(a) in the ESM), demonstrating that these materials have the ability to store hydrogen [43]. The adsorption of hydrogen in these materials follows two mechanisms: physisorption and chemisorption. The former often occurs at low temperature and high pressure. The hydrogen storing ability of Au/ZSBA-PL is much higher than those of Au/ZSBA-RD and Au/ZSBA-HP, whereas the hydrogen storing abilities of Au/ZSBA-RD and Au/ZSBA-HP are similar, indicating that the ZrO_2 confined in Au/ZSBA-PL may contribute to the storage of hydrogen. In addition, three peaks appear in the range from 400 to 600 °C for Au/ZSBA-PL, and only two peaks are present in the Au/ZSBA-RD and Au/ZSBA-HP samples in the temperature range of 300 to 550 °C, which demonstrates that the immobilization of ZrO_2 on Au/ZSBA-PL not only greatly increases the amount

of H_2 desorption, but also increases the desorption temperature.

The H_2-TPR results were considered a reflection of the reducibility of metallic ions with high valence, converted into ions with low valence or into metallic atoms [44]. Therefore, the temperature of the reduction peak in the Au/ZSBA materials can be used as a measure of the redox ability of the materials. There is no reduction peak below 300 ˚C for Au/ZSBA-PL-100 and Au/ZSBA-PL-350 (Fig. S1(b) in the ESM), demonstrating that all the gold species of Au/ZSBA-PL are metallic atoms. In comparison with Au/ZSBA-PL, the TPR profiles of Au/ZSBA-RD and Au/ZSBA-HP show a broad weak peak below 200 ˚C, indicating that a small amount of gold ion species exists in these materials. The above results prove that the introduction of ZrO_2 in Au/ZSBA-PL contributes to the reduction of cationic Au species into metallic atoms.

3.2 Catalytic performance for the reduction of 4-NP

The activity of the as-synthesized gold catalysts Au/ZSBA with different morphologies was evaluated for the reduction of 4-NP in the presence of $NaBH_4$. It is well known that 4-NP possesses a strong absorption band at ~317 nm, which is remarkably red-shifted to 400 nm after the introduction of $NaBH_4$ due to the formation of nitrophenolate ions [45]. During the reaction process, the conversion of 4-NP was detected in the form of 4-nitrophenolate anions through UV–vis spectrophotometry. The catalytic performance of Au/ZSBA with different morphologies and that of Au/SBA-15 prepared by incipient wetness impregnation were comparatively studied, and the results are shown in Fig. 9. It can be observed that there is a decrease in the absorbance of the 4-nitrophenolate anion at 400 nm, associated with the concomitant evolution of the product (4-AP) peak at 295 nm, demonstrating that 4-NP was successfully reduced to 4-AP. The conversion of 4-NP was calculated as C_t/C_0, where C_t and C_0 denote the 4-NP concentration at time t and 0, respectively. The value of C_t/C_0 was determined by the relative intensity of the absorbance (A_t/A_0) at 400 nm. Figures 9(a)–9(d) illustrate the absorbance versus reaction time plots for the 4-NP reduction by the Au/ZSBA catalysts with different morphologies. In the presence of Au/SBA-15, the adsorption band at 400 nm remained almost unchanged even after 20 min, which may be a result of the relatively large Au

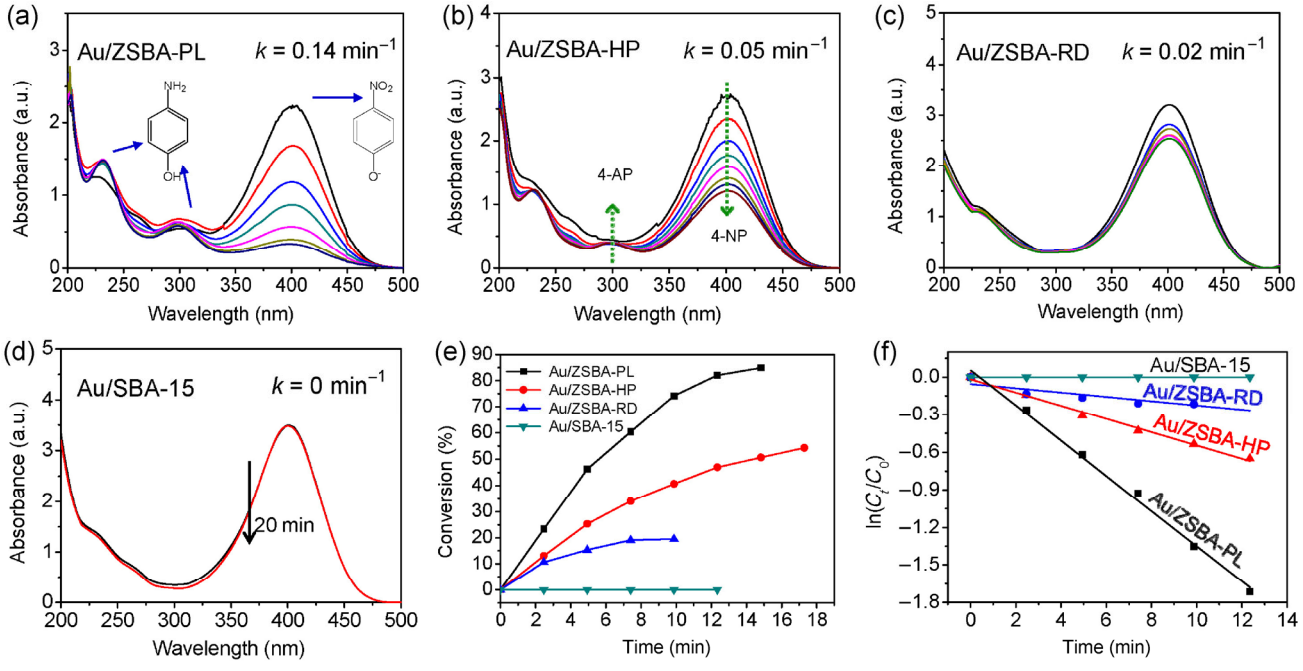

Figure 9 The reduction of 4-NP in aqueous solution recorded every 2.47 min over (a) Au/ZSBA-PL, (b) Au/ZSBA-HP, (c) Au/ZSBA-RD, and (d) Au/SBA-15. (e) Time dependent conversion of 4-NP over these catalysts. (f) The relationship between reaction time (min) and $\ln(C_t/C_0)$ for the catalysts.

nanoparticles (9.3 nm) in this catalyst. The reduction reaction proceeded rapidly for Au/ZSBA-PL. Figure 9(e) describes the conversion of 4-NP over the catalysts as a function of time (min), revealing that the reactivity of these catalysts follows the sequence: Au/SBA-15 < Au/ZSBA-RD < Au/ZSBA-HP < Au/ZSBA-PL. The reduction of 4-NP was assumed to be a pseudo-first order reaction with regard to 4-NP, since the amount of $NaBH_4$ greatly exceeds that of 4-NP. The linear relationship between the reaction time (min) and $\ln(C_t/C_0)$ for the catalysts listed in Fig. 9(f) matches well what would be expected from first-order kinetics. The reaction rate constants (k, min^{-1}) are summarized in Table S2 (see the ESM) and Fig. 9. The k values of these catalysts follow the order: Au/SBA-15 (0 min^{-1}) < Au/ZSBA-RD (0.02 min^{-1}) < Au/ZSBA-HP (0.05 min^{-1}) < Au/ZSBA-PL (0.14 min^{-1}). The Au nanoparticles of all the Au/ZSBA catalysts have a similar size. Therefore, the different activities of Au/ZSBA-RD, Au/ZSBA-HP, and Au/ZSBA-PL seem to be related to the pore size and length of the mesochannels inside the catalysts. Au/ZSBA-PL, with short mesochannels (210 nm) and large pore diameter (6.7 nm), exhibits high diffusion ability, resulting in an excellent performance towards 4-NP reduction. In contrast, Au/ZSBA-RD and Au/ZSBA-HP exhibit relatively inferior catalytic activities, which may be attributed to their long mesochannels (≥750 nm) and relatively small pore diameter (≤6.0 nm). In addition, the effect of the Au/ZSBA thickness on the 4-NP reduction is correlated to that of the mesochannel and pore diameter. The schematic representation of the catalytic performance of the Au/ZSBA catalysts with different morphologies is displayed in Scheme 2.

Besides the morphologies and mesochannels of the supports, the effect of the gold nanoparticle size on the reduction of 4-NP was also investigated. A series of Au nanoparticles were obtained with Au/ZSBA-PL calcined at different temperatures. The catalytic results of the 4-NP reduction over Au/ZSBA-PL with gold nanoparticles of different sizes are listed in Fig. 10 and Table S2 (in the ESM). Although the surface area and pore structure of Au/ZSBA-PL-100, Au/ZSBA-PL-200, Au/ZSBA-PL-350, and Au/ZSBA-PL-550 display little differences, which may also influence their catalytic performance, the main influencing factor

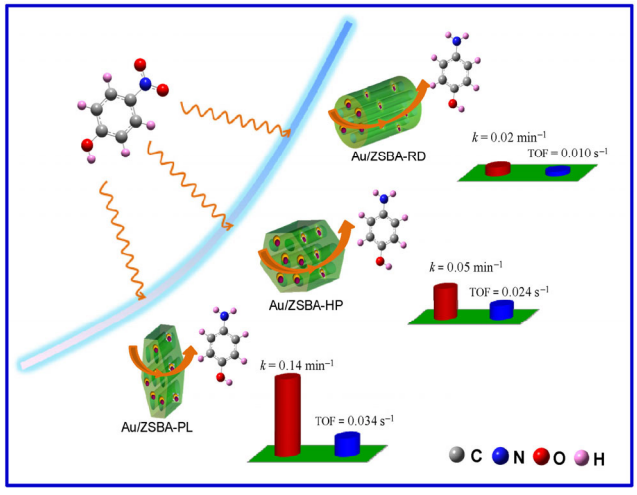

Scheme 2 Schematic representation of the catalytic performance for the Au/ZSBA catalysts with different morphologies.

here is the size of the gold nanoparticles in the Au/ZSBA-PL catalysts. With the increasing Au nanoparticle size, the catalytic performance of Au/ZSBA-PL first increases and then decreases. Among the catalysts, Au/ZSBA-PL-350 exhibits the best reaction rate constant (0.14 min^{-1}), demonstrating that Au nanoparticles of 4.0 nm in size are the most suitable for the reduction of 4-NP. Au/ZSBA-PL-100, with a Au nanoparticle size below 1 nm, shows a poor catalytic performance (k = 0.03 min^{-1}) which may be attributed to the poor storage ability of electronic for ultrafine Au nanoparticles. Moreover, Au/ZSBA-PL-550 (calcined at 550 ℃) also possesses inferior catalytic activity towards 4-NP reduction (k = 0.05 min^{-1}), which may be attributed to a lower number of surface active sites in large Au nanoparticles.

To further compare the catalytic performance of these catalysts, the values of TOF (s^{-1}) and rate constant K ($min^{-1}\cdot g^{-1}$) were calculated over the total weight of the gold catalysts, and the results are listed in Table S2 and Fig. S2 (see the ESM). As observed in Fig. S2(a), the TOF (s^{-1}) and rate constant K ($min^{-1}\cdot g^{-1}$) values are closely related to the morphologies of the catalysts; among them, Au/ZSBA-PL exhibits excellent K (141.3 $min^{-1}\cdot g^{-1}$) and TOF (0.0341 s^{-1}) values. In addition, the size of the Au nanoparticles has also an effect on the performance of the catalysts, as displayed in Fig. S2(b) (see the ESM). The catalyst with Au nanoparticle size of 4.0 nm exhibits the highest rate constant K (141.3 $min^{-1}\cdot g^{-1}$) and TOF (0.0341 s^{-1}) among all the catalysts,

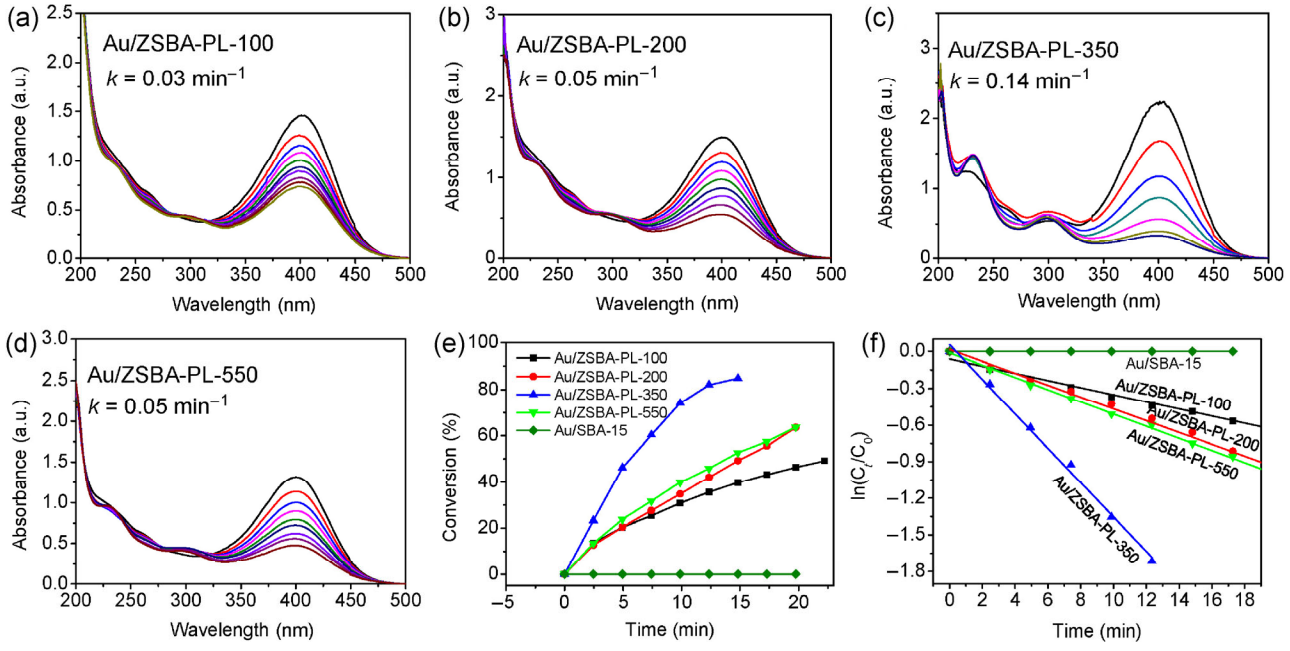

Figure 10 The reduction of 4-NP in aqueous solution recorded every 2.47 min with (a) Au/ZSBA-PL-100, (b) Au/ZSBA-PL-200, (c) Au/ZSBA-PL-350, and (d) Au/ZSBA-PL-550. (e) Conversion of 4-NP over the catalysts as a function of time. (f) The relationship between $\ln(C_t/C_0)$ and reaction time (min) for various catalysts.

while the K and TOF values of the catalysts with Au particle size of 0.9 or 7.2 nm are relatively lower. Moreover, the trends in the TOF and K values relative to the morphology and Au nanoparticle size of these catalysts are quite similar.

3.3 Effect of the reaction parameters on the reduction of 4-NP

The effect of the reaction parameters (including the catalyst loading and the concentration of 4-NP and the reducing agent $NaBH_4$) on the reduction of 4-NP were systematical investigated. In order to understand the catalytic efficiency, the amount of catalyst was varied while maintaining constant concentrations of 4-NP (0.0001 M) and $NaBH_4$ (0.01 M). As illustrated in Fig. S3(a) (see the ESM), with the increasing reaction time, the ratio of the absorbance at time t (A_t) to that at t = 0 (A_0) decreased. Since the absorbance of 4-NP is proportional to its concentration in the reaction solution, A_t/A_0 represents the ratio of the concentration of 4-NP during the reaction. The data in Fig. S3(b) and Table S3 (see the ESM) demonstrate that the conversion of 4-NP increases with the reaction time, and that the reaction rate is also enhanced by increasing the catalyst loading. Herein, the reduction reaction follows pseudo-first order kinetics. According to Ref. [46], the reaction rate increases linearly with the amount of catalyst in the case of heterogeneous catalytic reactions. The reduction of 4-NP over the Au/ZSBA catalysts with different morphologies also shows that there is a linear relationship between the reaction rates and the catalyst loading (Fig. S3(d) in the ESM). These results demonstrate that an increase in the amount of catalyst results in more reaction sites and a larger surface area, thus increasing more reaction to occur as well as the reaction rate.

The optimum concentration of $NaBH_4$ for this reaction was found by varying the concentration of $NaBH_4$ with the concentration of 4-NP (0.0001 M) while maintaining a fixed amount of catalyst (1 mg). A series of experiments over Au/ZSBA-PL-350 (Fig. S4 in the ESM) revealed that the conversion of 4-NP increases with the increasing concentration of $NaBH_4$. It can be seen (Table S4 and Fig. S4(d)) that the reaction rate increases fast with the concentration of $NaBH_4$ in the range from 0.002 to 0.01 M, and remains almost unchanged once the concentration reaches 0.01 M. In addition, the TOF of the reaction over Au/ZSBA-PL-

350 also increases with the increasing concentration of $NaBH_4$, with a trend that is similar to that of the reaction rate. The above results indicate that the reaction rate and TOF are almost independent on the concentration of $NaBH_4$ at concentrations above 0.01 M.

In order to investigate the effect of the concentration of 4-NP, reduction experiments were performed by varying the concentration of 4-NP while keeping the concentration of $NaBH_4$ (0.01 M) and the amount of catalyst (1 mg) fixed. As shown in Figs. S5(a) and S5(b) (in the ESM), the conversion of 4-NP decreases with the increasing initial concentration of 4-NP. Figure S5(c) (in the ESM) reveals almost linear plots for $\ln(C_t/C_0)$ versus reaction time (min), satisfying the conditions of pseudo-first order kinetics. The reaction rate constant k (min^{-1}) measurements (Table S4 and Fig. S5(d) in the ESM) demonstrate that the rate constant is directly dependent on the initial concentration of 4-NP, and decreases with the increasing concentration of 4-NP. These results can be attributed to the competition between the reactants over the free sites on the gold nanoparticle surface. The reduction reaction can only take place between reactants adsorbed on the catalyst surface, and any excess reagents may decrease the overall rate.

In summary, the reaction parameters (including the catalyst loading, and the concentration of 4-NP and the reducing agent $NaBH_4$) have an influence on the rate of this reduction reaction. In addition, the stability of the Au/ZSBA catalysts was investigated by evaluating the performance of Au/ZSBA-PL in the reduction of 4-NP for four cycles with the same reaction time (~15 min). The catalytic results show that the conversion of 4-NP decreases by 9.8% after five cycling reactions (Fig. S6 in the ESM). The TEM images show that the gold nanoparticles are well retained and that there is no agglomeration after several catalytic cycles, demonstrating the high stability and reusability of the as-synthesized Au/ZSBA-PL catalyst.

3.4 Mechanistic insight of the reduction process over the Au/ZSBA catalysts

Based on the above results and Refs. [47–49], a mechanism for the reduction of 4-NP to 4-AP by $NaBH_4$ over the Au/ZSBA catalysts is proposed in Scheme 3 according to the Langmuir–Hinshelwood mechanism, where both reactants are adsorbed on the catalyst surface prior to the reaction. Herein, the possible mechanism for the 4-NP reduction involves some crucial steps: (a) $NaBH_4$ is decomposed by hydrolysis; then, the active hydrogen and electrons formed from $NaBH_4$ are transferred to the Au nanoparticles and adsorbed on their surface. (b) 4-NP is adsorbed on the surface of the Au nanoparticles through chemical interactions, forming a surface complex. (c) The reduction of 4-NP by the active hydrogen and electrons adsorbed on the Au nanoparticle surface results in the adsorbed product 4-AP. (d) Desorption of the products from the surface of the catalyst. Of all the steps, the reaction of the adsorbed species is the rate-determining step, and the adsorption–desorption equilibrium follows a Langmuir isotherm. The whole reaction process for the reduction of 4-NP includes the following equations

$$BH_4^- + 2H_2O \longrightarrow BO_2^- + 4H_2\uparrow \quad (5)$$

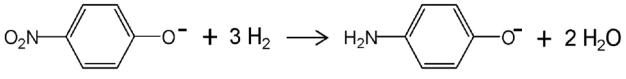

(6)

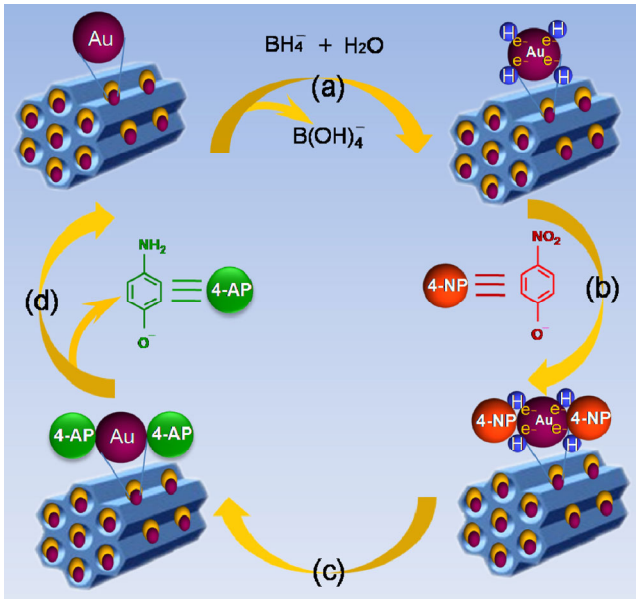

Scheme 3 Mechanistic model of the Langmuir–Hinshelwood mechanism for the reduction of 4-NP to 4-AP by $NaBH_4$ in the presence of Au/ZSBA catalysts.

4 Conclusions

In this research, a mercaptosilane-assisted strategy for the synthesis of a series of novel gold catalysts consisting of gold nanoparticles within a micro-mesoporous ZSBA material is reported. The as-synthesized Au/ZSBA catalysts present hexagonal-prism, rod, or platelet morphologies as a result of controlling the synthetic raw material and the reaction conditions. The gold nanoparticles confined in the Au/ZSBA framework exhibit strong interactions with the support. Among the Au/ZSBA catalysts with different morphologies, the platelet-shaped material (Au/ZSBA-PL), with short mesochannels (210 nm) and large pore diameter (6.7 nm), exhibits high catalytic performance in the reduction of 4-NP, while the hexagonal-prism-shaped (Au/ZSBA-HP) and rod-shaped (Au/ZSBA-RD) catalysts, with long mesochannels and relative smaller pore sizes, show poor catalytic activity. In the case of Au/ZSBA-PL, the Au/ZSBA-PL-350 sample with Au particle size of 4.0 nm exhibits the highest reaction rate constant (0.14 min^{-1}), and is the most suitable catalyst for the reduction of 4-NP. The presence of Au@zeolite seeds within the framework of the mesoporous material with platelet morphology results in outstanding physicochemical properties and catalytic performance, and the materials here reported are a promising alternative for the disposal of nitroaromatic compounds.

Acknowledgements

This work was financially supported by the National Natural Science Foundation of China (Nos. 21573286, 21576288, and 21276277), the Ministry of Science and Technology of China (Nos. 2011BAK15B05 and 2015AA034603), the Specialized Research Fund for the Doctoral Program of Higher Education (No. 20130007110003), Science Foundation of China University of Petroleum, Beijing (No. 2462015YQ0304).

Electronic Supplementary Material: Supplementary material (catalytic results and characterization analysis of these catalysts) is available in the online version of this article at http://dx.doi.org/10.1007/s12274-016-1193-8.

References

[1] Hervés, P.; Pérez-Lorenzo, M.; Liz-Marzán, L. M.; Dzubiella, J.; Lu, Y.; Ballauff, M. Catalysis by metallic nanoparticles in aqueous solution: Model reactions. *Chem. Soc. Rev.* **2012**, *41*, 5577–5587.

[2] Kovach, I. M.; Enyedy, E. J. Active-site-dependent elimination of 4-nitrophenol from 4-nitrophenyl alkylphosphonyl serine protease adducts. *J. Am. Chem. Soc*. **1998**, *120*, 258–263.

[3] Gao, D. W.; Duan, A. J.; Zhang, X.; Chi, K. B.; Zhao, Z.; Li, J. M.; Qin, Y. C.; Wang, X. L.; Xu, C. M. Self-assembly of monodispersed hierarchically porous Beta-SBA-15 with different morphologies and its hydro-upgrading performances for FCC gasoline. *J. Mater. Chem. A* **2015**, *3*, 16501–16512.

[4] Gao, D. W.; Duan, A. J.; Zhang, X.; Zhao, Z.; E, H.; Li, J. M.; Wang, H. Synthesis of NiMo catalysts supported on mesoporous Al-SBA-15 with different morphologies and their catalytic performance of DBT HDS. *Appl. Catal. B* **2015**, *165*, 269–284.

[5] Guo, H. F.; Yan, X. L.; Zhi, Y.; Li, Z. W.; Wu, C.; Zhao, C. L.; Wang, J.; Yu, Z. X.; Ding, Y.; He, W.; Li, Y. D. Nanostructuring gold wires as highly durable nanocatalysts for selective reduction of nitro compounds and azides with organosilanes. *Nano Res.* **2015**, *8*, 1365–1372.

[6] Zhang, J.; Liu, Y.; Lv, J.; Li, G. X. A colorimetric method for α-glucosidase activity assay and its inhibitor screening based on aggregation of gold nanoparticles induced by specific recognition between phenylenediboronic acid and 4-aminophenyl-α-d-glucopyranoside. *Nano Res.* **2015**, *8*, 920–930.

[7] Zhang, X.; Corma, A. Supported gold(III) catalysts for highly efficient three-component coupling reactions. *Angew. Chem., Int. Ed.* **2008**, *47*, 4358–4361.

[8] Li, Z.-X.; Xue, W.; Guan, B.-T.; Shi, F.-B.; Shi, Z.-J.; Jiang, H.; Yan, C.-H. A conceptual translation of homogeneous catalysis into heterogeneous catalysis: Homogeneous-like heterogeneous gold nanoparticle catalyst induced by ceria supporter. *Nanoscale* **2013**, *5*, 1213–1220.

[9] Arcadi, A.; Bianchi, G.; Di Giuseppe, S.; Marinelli, F. Gold catalysis in the reactions of 1,3-dicarbonyls with nucleophiles. *Green Chem.* **2003**, *5*, 64–67.

[10] Gao, D. W.; Zhang, X.; Yang, Y.; Dai, X. P.; Sun, H.; Qin, Y. C.; Duan, A. J. Supported single Au(III) ion catalysts for high performance in the reactions of 1,3-dicarbonyls with alcohols. *Nano Res.* **2016**, *9*, 985–995.

[11] Sarkar, S.; Balisetty, L.; Shanbogh, P. P.; Peter, S. C. Effect of ordered and disordered phases of unsupported Ag_3In nanoparticles on the catalytic reduction of *p*-nitrophenol. *J. Catal.* **2014**, *318*, 143–150.

[12] Cárdenas-Lizana, F.; Lamey, D.; Perret, N.; Gómez-Quero, S.; Kiwi-Minsker, L.; Keane, M. A. Au/Mo_2N as a new catalyst formulation for the hydrogenation of *p*-chloronitrobenzene in both liquid and gas phases. *Catal. Commun.* **2012**, *21*, 46–51.

[13] Guan, B. Y.; Wang, T.; Zeng, S. J.; Wang, X.; An, D.; Wang, D. M.; Cao, Y.; Ma, D. X.; Liu, Y. L.; Huo, Q. S. A versatile cooperative template-directed coating method to synthesize hollow and yolk-shell mesoporous zirconium titanium oxide nanospheres as catalytic reactors. *Nano Res.* **2014**, *7*, 246–262.

[14] Chang, Y.-C.; Chen, D.-H. Catalytic reduction of 4-nitrophenol by magnetically recoverable Au nanocatalyst. *J. Hazard. Mater.* **2009**, *165*, 664–669.

[15] Chiou, J.-R.; Lai, B.-H.; Hsu, K.-C.; Chen, D.-H. One-pot green synthesis of silver/iron oxide composite nanoparticles for 4-nitrophenol reduction. *J. Hazard. Mater.* **2013**, *248–249*, 394–400.

[16] Sahiner, N.; Ozay, H.; Ozay, O.; Aktas, N. A soft hydrogel reactor for cobalt nanoparticle preparation and use in the reduction of nitrophenols. *Appl. Catal. B* **2010**, *101*, 137–143.

[17] Oturan, M. A.; Peiroten, J.; Chartrin, P.; Acher, A. J. Complete destruction of *p*-nitrophenol in aqueous medium by electro-fenton method. *Environ. Sci. Technol.* **2000**, *34*, 3474–3479.

[18] Modirshahla, N.; Behnajady, M. A.; Mohammadi-Aghdam, S. Investigation of the effect of different electrodes and their connections on the removal efficiency of 4-nitrophenol from aqueous solution by electrocoagulation. *J. Hazard. Mater.* **2008**, *154*, 778–786.

[19] Hu, H. W.; Xin, J. H.; Hu, H.; Wang, X. W. Structural and mechanistic understanding of an active and durable graphene carbocatalyst for reduction of 4-nitrophenol at room temperature. *Nano Res.* **2015**, *8*, 3992–4006.

[20] Xiong, W.; Sikdar, D.; Yap, L. W.; Guo, P. Z.; Premaratne, M.; Li, X. Y.; Cheng, W. L. Matryoshka-caged gold nanorods: Synthesis, plasmonic properties, and catalytic activity. *Nano Res.* **2016**, *9*, 415–423.

[21] Xia, Y. Y.; Shi, Z. Q.; Lu, Y. Gold microspheres with hierarchical structure/conducting polymer composite film: Preparation, characterization and application as catalyst. *Polymer* **2010,** *51*, 1328–1335.

[22] Zhang, M. M.; Liu, L.; Wu, C. L.; Fu, G. Q.; Zhao, H. Y.; He, B. L. Synthesis, characterization and application of well-defined environmentally responsive polymer brushes on the surface of colloid particles. *Polymer* **2007**, *48*, 1989–1997.

[23] Chang, G. H.; Luo, Y. L.; Lu, W. B.; Qin, X. Y.; Asiri, A. M.; Al-Youbi, A. O.; Sun, X. P. Ag nanoparticles decorated polyaniline nanofibers: Synthesis, characterization, and applications toward catalytic reduction of 4-nitrophenol and electrochemical detection of H_2O_2 and glucose. *Catal. Sci. Technol.* **2012**, *2*, 800–806.

[24] Pozun, Z. D.; Rodenbusch, S. E.; Keller, E.; Tran, K.; Tang, W. J.; Stevenson, K. J.; Henkelman, G. A systematic investigation of *p*-nitrophenol reduction by bimetallic dendrimer encapsulated nanoparticles. *J. Phys. Chem. C* **2013**, *117*, 7598–7604.

[25] Wang, P.-P.; Yu, Q. Y.; Long, Y.; Hu, S.; Zhuang, J.; Wang, X. Multivalent assembly of ultrasmall nanoparticles: One-, two-, and three-dimensional architectures of 2 nm gold nanoparticles. *Nano Res.* **2012**, *5*, 283–291.

[26] Gao, D. W.; Zheng, A. M.; Zhang, X.; Sun, H.; Dai, X. P.; Yang, Y.; Wang, H.; Qin, Y. C.; Xu, S. T.; Duan, A. J. Mercaptosilane-assisted synthesis of sub-nanosized Pt particles within hierarchically porous ZSM-5/SBA-15 materials and their enhanced hydrogenation properties. *Nanoscale* **2015**, *7*, 10918–10924.

[27] Chen, J. C.; Zhang, R. Y.; Han, L.; Tu, B.; Zhao, D. Y. One-pot synthesis of thermally stable gold@mesoporous silica core-shell nanospheres with catalytic activity. *Nano Res.* **2013**, *6*, 871–879.

[28] Katiyar, A.; Yadav, S.; Smirniotis, P. G.; Pinto, N. G. Synthesis of ordered large pore SBA-15 spherical particles for adsorption of biomolecules. *J. Chromatogr. A* **2006**, *1122*, 13–20.

[29] Chen, S.-Y.; Tang, C.-Y.; Chuang, W.-T.; Lee, J.-J.; Tsai, Y.-L.; Chan, J. C. C.; Lin, C.-Y.; Liu, Y.-C.; Cheng, S. A facile route to synthesizing functionalized mesoporous SBA-15 materials with platelet morphology and short mesochannels. *Chem. Mater.* **2008**, *20*, 3906–3916.

[30] Kang, Y. J.; Murray, C. B. Synthesis and electrocatalytic properties of cubic Mn−Pt nanocrystals (nanocubes). *J. Am. Chem. Soc.* **2010**, *132*, 7568–7569.

[31] Zhao, D. Y.; Feng, J. L.; Huo, Q. S.; Melosh, N.; Fredrickson, G. H.; Chmelka, B. F.; Stucky, G. D. Triblock copolymer syntheses of mesoporous silica with periodic 50 to 300 angstrom pores. *Science* **1998**, *279*, 548–552.

[32] Yu, Y.; Xiong, G.; Li, C.; Xiao, F.-S. Characterization of aluminosilicate zeolites by UV Raman spectroscopy. *Micro. Meso. Mater.* **2001**, *46*, 23–34.

[33] Knops-Gerrits, P.-P.; De Vos, D. E.; Feijen, E. J. P.; Jacobs, P. A. Raman spectroscopy on zeolites. *Microporous Mater.* **1997**, *8*, 3–17.

[34] Borodko, Y.; Ager, J. W.; Marti, G. E.; Song, H.; Niesz, K.; Somorjai, G. A. Structure sensitivity of vibrational spectra of mesoporous silica SBA-15 and Pt/SBA-15. *J. Phys. Chem. B* **2005**, *109*, 17386–17390.

[35] Jiang, J. L.; Yang, Y.; Duanmu, C.; Xu, Y.; Feng, L. D.; Gu, X.; Chen, J. Preparation of hollow ZSM-5 crystals in the presence of polyacrylamide. *Micro. Meso. Mater.* **2012**, *163*, 11–20.

[36] Liu, G. P.; Xiangli, F.; Wei, W.; Liu, S. N.; Jin, W. Q. Improved performance of PDMS/ceramic composite pervaporation membranes by ZSM-5 homogeneously dispersed in PDMS via a surface graft/coating approach. *Chem. Eng. J.* **2011**, *174*, 495–503.

[37] Panpa, W.; Jinawath, S. Synthesis of ZSM-5 zeolite and silicalite from rice husk ash. *Appl. Catal. B* **2009**, *90*, 389–394.

[38] Melero, J. A.; Stucky, G. D.; van Grieken, R.; Morales, G. Direct syntheses of ordered SBA-15 mesoporous materials containing arenesulfonic acid groups. *J. Mater. Chem.* **2002**, *12*, 1664–1670.

[39] Lévy, R.; Thanh, N. T. K.; Doty, R. C.; Hussain, I.; Nichols, R. J.; Schiffrin, D. J.; Brust, M.; Fernig, D. G. Rational and combinatorial design of peptide capping ligands for gold nanoparticles. *J. Am. Chem. Soc.* **2004**, *126*, 10076–10084.

[40] Ojea-Jiménez, I.; Puntes, V. Instability of cationic gold nanoparticle bioconjugates: The role of citrate ions. *J. Am. Chem. Soc.* **2009**, *131*, 13320–13327.

[41] Zhang, T.; Liu, J.; Wang, D. X.; Zhao, Z.; Wei, Y. C.; Cheng, K. Y.; Jiang, G. Y.; Duan, A. J. Selective catalytic reduction of NO with NH_3 over HZSM-5-supported Fe–Cu nanocomposite catalysts: The Fe–Cu bimetallic effect. *Appl. Catal. B* **2014**, *148–149*, 520–531.

[42] Yuan, J.; Huang, X.; Chen, M. X.; Shi, J. W.; Shangguan, W. F. Ozone-assisted photocatalytic degradation of gaseous acetaldehyde on TiO_2/M-ZSM-5 (M = Zn, Cu, Mn). *Catal. Today* **2013**, *201*, 182–188.

[43] Zhang, X.; Shi, H.; Xu, B.-Q. Vital roles of hydroxyl groups and gold oxidation states in Au/ZrO_2 catalysts for 1,3-butadiene hydrogenation. *J. Catal.* **2011**, *279*, 75–87.

[44] Wei, Y. C.; Liu, J.; Zhao, Z.; Duan, A. J.; Jiang, G. Y. The catalysts of three-dimensionally ordered macroporous $Ce_{1-x}Zr_xO_2$-supported gold nanoparticles for soot combustion: The metal–support interaction. *J. Catal.* **2012**, *287*, 13–29.

[45] Lin, Y. Y.; Qiao, Y.; Wang, Y. J.; Yan, Y.; Huang, J. B. Self-assembled laminated nanoribbon-directed synthesis of noble metallic nanoparticle-decorated silica nanotubes and their catalytic applications. *J. Mater. Chem.* **2012**, *22*, 18314–18320.

[46] Panigrahi, S.; Basu, S.; Praharaj, S.; Pande, S.; Jana, S.; Pal, A.; Ghosh, S. K.; Pal, T. Synthesis and size-selective catalysis by supported gold nanoparticles: Study on heterogeneous and homogeneous catalytic process. *J. Phys. Chem. C* **2007**, *111*, 4596–4605.

[47] Zhang, H. J.; Li, X. Y.; Chen, G. H. Ionic liquid-facilitated synthesis and catalytic activity of highly dispersed Ag nanoclusters supported on TiO_2. *J. Mater. Chem.* **2009**, *19*, 8223–8231.

[48] Xu, W. L.; Kong, J. S.; Yeh, Y. T. E.; Chen, P. Single-molecule nanocatalysis reveals heterogeneous reaction pathways and catalytic dynamics. *Nat. Mater.* **2008**, *7*, 992–996.

[49] Yang, Y.; Zhang, W.; Zhang, Y.; Zheng, A. M.; Sun, H.; Li, X. S.; Liu, S. Y.; Zhang, P. F.; Zhang, X. A single Au nanoparticle anchored inside the porous shell of periodic mesoporous organosilica hollow spheres. *Nano Res.* **2015**, *8*, 3404–3411.